Roser Anna (Orcid ID: 0000-0002-5184-2916)
Glenn Nancy F. (Orcid ID: 0000-0003-2124-7654)
Caughlin T. Trevor (Orcid ID: 0000-0001-6752-2055)

Methods, Tools, and Technologies

Drone imagery protocols to map vegetation are transferable between dryland sites across an elevational gradient

Anna Roser[1]

Josh Enterkine[2]

Juan M. Requena-Mullor[3]

Nancy F Glenn[2]

Alex Boehm[4]

Marie-Anne de Graaff[1]

Pat Clark[4]

Fred Pierson[4]

T. Trevor Caughlin[1]†

[1]Department of Biological Sciences, Boise State University, [2]Department of Geosciences, Boise State University, [3]School for Environment and Sustainability, University of Michigan, [4]Northwest Watershed Research Center, USDA Agricultural Research Service,

†Corresponding author: trevorcaughlin@boisestate.edu

Handling Editor: Debra P. C. Peters

This is the author manuscript accepted for publication and has undergone full peer review but has not been through the copyediting, typesetting, pagination and proofreading process, which may lead to differences between this version and the Version of Record. Please cite this article as doi: 10.1002/ecs2.4330

ABSTRACT

The structure and composition of plant communities in drylands are highly variable across scales, from microsites to landscapes. Fine spatial resolution field surveys of dryland plants are essential to unravel the impact of climate change; however, traditional field-data collection is challenging considering sampling efforts and costs. Unoccupied Aerial Systems (UAS) can alleviate this challenge by providing standardized measurements of plant community attributes with high resolution. However, given widespread heterogeneity in plant communities in drylands, and especially across environmental gradients, the transferability of UAS imagery protocols is unclear. Plant functional types (PFTs) are a classification scheme that aggregates the diversity of plant structure and function. We mapped and modeled PFTs and fractional photosynthetic cover using the same UAS imagery protocol across three dryland communities, differentiated by a landscape-scale gradient of elevation and precipitation. We compared the accuracy of the UAS products between the three dryland sites. PFT classifications and modeled photosynthetic cover had highest accuracies at higher elevations (2,241m) with denser vegetation. The lowest site (1,101m), with more bare ground, had the least agreement with the field data. Notably, shrub cover was well predicted across the gradient of elevation and precipitation (~230-1,100 mm/year). UAS surveys captured the heterogeneity of plant cover across sites and presented options to measure leaf-level composition and structure at landscape levels. Our results demonstrate that some PFTs (i.e. shrubs) can readily be detected across sites using the same UAS imagery protocols, while others (i.e. grasses) may require site-specific flight protocols for best accuracy. As UAS are increasingly used to monitor dryland vegetation, developing protocols that maximize information and efficiency is a research and management priority.

Keywords: unoccupied aerial vehicles, fractional photosynthetic cover, remote sensing

INTRODUCTION

Dryland ecosystems represent 41% of the global land surface, and the global extent of drylands is expected to increase by 7% over the next 60 years (Koutroulis 2019). Given the extensive land area cover of drylands, they have a significant impact on the global carbon cycle (Poulter et al. 2014). The composition of dryland plant communities fundamentally impacts their role in the global carbon cycle, because plants regulate photosynthetic rates and soil processes, both of which are foundational to net carbon exchange between ecosystems and the atmosphere (Breulmann et al. 2012, Ning et al. 2021). Dryland ecosystems are also being impacted by climate change, as well as a myriad of other human disturbances, leading to rapid changes in structure and biogeochemical cycles in these ecosystems (Renne et al. 2019, Philip et al. 2021). In light of their global importance, long-term monitoring has played an essential role in identifying vegetation dynamics in drylands with relevance for land management and restoration (Shriver et al. 2019, Vivoni et al. 2021).

Unoccupied Aerial Systems (UAS) can support vegetation monitoring by measuring plant communities across large spatial extents with high resolution imagery. High spatial resolution imagery (e.g. pixels < 1 cm^2) has particular utility in drylands ecosystems where key vegetation communities, such as soil biocrust and annual grasses, vary at fine spatial grains (Beckstead et al. 2010, Chen et al. 2020). Applications of UAS-derived aerial imagery in dryland ecosystems include detection of rare and threatened species (Rominger and Meyer 2019), mapping vegetation functional groups (Wood et al. 2022), quantifying impacts of grazing treatments (Polley et al. 2022), and measuring habitat quality for wildlife (Olsoy et al. 2018). UAS offers

potential cost and efficiency advantages over field-based or other remote sensing-based approaches. UAS are easily deployable, less expensive, and collect higher spatial resolution imagery than other airborne platforms (Koh and Wich 2012). Integrating UAS imagery into vegetation monitoring plans will advance ecological studies of dryland ecosystems.

The potential for UAS imagery to supplement ongoing field campaigns raises questions on how these novel data can be compared across disparate sites and related to historical field data. Exploration of UAS approaches is required to understand the efficacy of generalizing flight protocols and image analysis across the wide range of environmental gradients within dryland landscapes. For example, if an UAS application across elevation and precipitation gradients requires a unique analysis to characterize each vegetation community, the efficiency of this application is far less promising. The utility of UAS imagery for understanding ecosystem change also raises the question of how UAS-derived vegetation data can be linked to ongoing and historic field data, such as vegetation monitoring plots (Gillan et al. 2020). In light of calls to include UAS flights in data collection plans for networks of long-term monitoring sites (Marvin et al. 2016, Kitzes et al. 2021), quantifying the interoperability of UAS imagery is paramount.

In this study, we compare and contrast UAS-derived metrics and field data from vegetation monitoring plots across an elevational gradient in the Northern Great Basin. Our study sites are located in the Reynold's Creek Critical Zone Observatory, a site with monitoring protocol broadly representative of long-term research networks, including the National Ecological Observatory Network (Brantley et al. 2017). Our UAS-derived metrics include dryland plant function types (PFTs) and fractional photosynthetic cover. PFTs are a classification scheme that aggregates the diversity of plant structure and function (Woodward and Cramer 1996). Examples of PFTs in drylands are grasses, forbs, shrubs, and in some cases, trees. We

also measured UAS-derived fractional photosynthetic cover, which is the amount of "green" canopy across a given landscape. We then evaluate correlations between UAS-derived vegetation metrics and field-based point-intercept sampling, a widely-used method for assessing plant species cover (Clark and Seyfried 2001). Furthermore, we assessed the efficacy of our UAS imagery collection protocols for mapping PFTs and fractional photosynthetic cover across three sites that vary in elevation and species composition. We evaluated the transferability of image protocols based on structure, density, and spectral features of each site. We use the term, "transferability" to describe the ability to apply the same UAS image protocols across an elevation and precipitation gradient. Our specific objectives were to: (1) Identify and map PFT's at each site; (2) Map fractional photosynthetic cover at each site; and then (3) compare the accuracy of the PFT and fractional photosynthetic map products between the sites along an elevation and precipitation gradient to assess the transferability of our protocols and methods.

METHODS

Study Sites

We conducted our research in the Reynolds Creek Experimental Watershed (RCEW), Idaho, USA. The RCEW encompasses an elevation and precipitation gradient (1,101-2,241 m and ~230-1,100 mm/year, respectively), representing the environmental heterogeneity that characterizes the sagebrush-steppe in the Northern Great Basin. In 2015, the USDA Agricultural Research Services (ARS) began data collection to assess the characteristics and long-term dynamics of sagebrush-steppe vegetation in the RCEW. Plot design and methods for vegetation surveys were based on guidance and procedures established by the U.S. Long-Term Agroecosystem Research (LTAR) network. Key metrics of vegetation diversity are measured

annually by field crews, including species abundance, species cover, photosynthetic cover, and dimensional measurements.

Data Collection

Vegetation field data were collected to provide a reference dataset to compare to the UAS image products. The data were collected in 2019 at three study sites crossing the elevation and precipitation gradient: Low, Middle, and High (Figure 1 and 2). Each site is characterized by the dominance of different sagebrush and other shrub species. Wyoming big sage (*Artemisia tridentata* ssp. *wyomingensis*) is the most common shrub species at the Low site, which has an elevation of 1,425 m. The Middle site has an elevation of 1,680 m and is characterized by low sage (*Artemisia arbuscula*) and co-dominant forbs, tailcup, and silvery lupine (*Lupinus caudatus* and *Lupinus argenteus*). At the High site, with an elevation of 2,110 m, mountain big sage (*Artemisia tridentata* ssp. *vaseyana*) and Utah snowberry (*Symphoricarpos oreophilus utahensis*) shrubs are co-dominant. Each site is 1 ha and contains 30 randomly distributed 1-m^2 field plots. The point-intercept sampling method (Clark and Seyfried 2001) was used at each field plot to collect data on plant species cover. A pin was lowered 100 times in each plot on a grid system; each time the pin made physical contact with vegetation, that contact was recorded to species-level. For example, one pin drop could make contact with several sagebrush leaves and stems, forb and/or grass leaves and stems, and the basal substrate. Each contact is recorded and coded as ‘green’ or ‘not green’. These data were used to estimate fractional photosynthetic cover and to identify PFTs. Fractional photosynthetic cover was calculated by taking the total number of "green" point intercepts or hits and dividing by the total number of hits in the plot. For this study, "green" hits were indicated when the sampling pin encountered photosynthetically active material.

We used a MicaSense RedEdge 3 sensor mounted on a DJI Matrice 600 Pro UAS platform to collect multispectral imagery of each site. The drone was flown by a Federal Aviation Administration (FAA) Part 107 certified remote pilot from June 5 – July 9 2019. To reduce shadowing, all flights were completed within two hours of solar noon. The RedEdge is a broadband multispectral sensor: blue (475nm), green (560nm), red (668nm), red edge (717nm), and near-infrared (840nm). The RedEdge sensor was radiometrically calibrated using a reflectance panel before and after each flight. We also flew a DJI Phantom 4 with the stock Red Green Blue (RGB) camera over each site to collect imagery at a finer spatial resolution to assist with training and test data for classification (Table 1). We used Universal Ground Control Software (UgCS v 3.2.113 SPH Engineering, Latvia) for all mission planning (Table 1). Thirteen ground control points (GCPs) were placed evenly within each study site. The location of all GCPs was recorded with a Real Time Kinematic GPS. Each flight was concurrent with field data collection. To aid in co-registration of imagery from the two sensors, flights at a given site were conducted on the same day using the same ground control points. All UAS data were pre-processed in Agisoft Metashape (v 1.5.5.9097, Agisoft LLC, St. Petersburg, Russia). For both sensors, all photos were aligned, filtered, and exported as georeferenced RGB and multispectral TIFFs (Table 1). The multispectral image products had resolutions of 3.5 cm GSD, and the RGB imagery had resolutions of 1cm GSD. Within each 1-m^2 field plot, there were about 800 pixels in the multispectral imagery.

Analysis

Mapping Plant Functional Types. To map the PFTs, we utilized a mean shift segmentation algorithm in ArcGIS Pro (v 2.7.3 ESRI, Redlands, CA, USA) with the RGB imagery, which resulted in a polygon layer over each site. We manually assigned corresponding polygons into

PFT categories. At all sites, PFT categories included bare ground, grass, and shrubs. At the Middle and High sites, PFT categories also included forbs and trees; cover within these categories was minimal to non-existent at the Low site. We then used the manually-assigned polygons, split into test and training datasets to run a random forest classification, in ArcGIS Pro. The classification was run only on the multispectral imagery and the result was a classified image of PFTs for each site (Figure 2).

Statistical analysis All statistical analyses were conducted in R (v 3.5.2) and RStudio (v 1.2.5001). Classification accuracy was assessed by comparing classified polygons to polygons that had been manually assigned PFTs. To compare percent cover from classified imagery to percent cover from point-intercept field plots, we used Spearman's Rank Sum correlation tests. The correlation tests used in this study are not to determine the "truth" of the imagery compared to the field data but a comparison between methods for quantifying PFT percent cover and fractional photosynthetic cover. Due to the difference in sampling density between the UAS imagery and field data, we would not expect these data to correlate precisely.

Mapping Fractional Photosynthetic Cover. To map fractional photosynthetic cover, we calculated multiple vegetation indices from the multispectral imagery. We tested the predictive ability of the Normalized Vegetation Index (NDVI), perhaps the most commonly-used vegetation index in remote sensing (Table 2). We also tested the predictive ability of two indices designed to minimize the reflectance of bare soil, common in dryland sites: optimized soil adjusted index (OSAVI) and modified soil adjusted index (MSAVI) (for a full list of tested vegetation indices, see Table 2).

To develop a metric for fractional photosynthetic cover, the PFT polygons developed using the mean shift algorithm were aggregated to "photosynthetic" or "non-photosynthetic"

classes based on the high resolution RGB imagery. Dead shrubs and soil are examples of non-photosynthetic categories, while live shrubs, grasses, and forbs were categorized as photosynthetic. For each classified polygon, we extracted the mean vegetation indices values. We used Log-Loss to calculate the vegetation index with the highest predictive accuracy for fractional photosynthetic cover. Log-Loss measures the uncertainty of fitted probabilities, in this case predicted fractional photosynthetic cover, by comparing them to observed data. For outcomes constrained between 0 and 1, log-loss is a proper scoring rule that enables comparisons of model performance on a continuous scale (Bickel 2007). Once we identified the top-performing vegetation index for each site, we used a Bayesian logistic regression to model the relationship between the vegetation index and fractional photosynthetic cover. We chose to use a Bayesian framework due to Bayesian models' utility for data assimilation and uncertainty propagation, including fusing vegetation indices with other ecologically-relevant data sources (Caughlin et al. 2021). We extracted the mean fractional photosynthetic cover for the field plots, so each plot had a ratio of green cover based on the pixels in the plot. We also calculated a ratio of green cover for each plot from the point intercept field data, based on the total number of hits vs. green hits. We then ran a Pearson's Correlation test between the photosynthetic cover ratios of the field plots and the imagery.

Comparing UAS imagery protocols. To evaluate the UAS image products among sites for PFTs, we compared the overall classification accuracies at each site and accuracies for individual classes, using manually-assigned polygons as validation data. We evaluated the overall classification accuracy for each site, as well as classification accuracies between sites to gauge if there were differences within a class between sites. We also considered the correlation tests between the field data and the UAS data. To evaluate maps of fractional photosynthetic cover, we used log-

loss to compare predictions of fractional photosynthetic cover between vegetation indices at each site. Additionally, we considered correlation tests between the field data and UAS maps of fractional photosynthetic cover.

RESULTS

Mapping plant functional types

We found strong correlations between UAS-derived PFT percent cover and field data, with the exception of the grass class, at the Middle and the High sites (Table 3). In contrast, correlations between UAS and field data were weak at the Low site. Overall, we found UAS data have, on average, 33% higher estimates of bare ground than field measurements. Additionally, estimates for grass cover from field data were 17% higher on average than UAS data. Lastly, both field and image methods agreed on low percent coverage for forbs (1-10%), and there was strong agreement between estimates of shrub percent cover (27% field, 30% images).

The overall PFT classification accuracies from the random forest of the multispectral data were similar for the three sites: the Low site (70%), the Middle site (73%), and the High site (78%). The highest PFT accuracies were obtained for the shrub class at all sites. Misclassification occurred mostly between ground and grass at all sites.

Mapping fractional photosynthetic cover

High accuracies of fractional photosynthetic cover were derived from all indices (Table 4). The MSAVI-based cover estimates had the highest predictive power, although differences between MSAVI and other indices were relatively small. Evaluating the MSAVI vegetation index relative to manually classified polygons, we were able to model fractional photosynthetic cover with accuracies of 80%, 64%, and 93% for the Low, Middle, and High sites, respectively. In addition, slope estimates from logistic regression indicated that MSAVI values had a significant positive relationship with fractional photosynthetic cover at all sites: 8.1 at the Low

site (95% CI: 7.7, 8.5); 3.2 at the Middle site (95% CI: 3.0, 3.5); and, 12.3 at the High site (95% CI: 11.0, 13.6). When we applied the model relationship with MSAVI to estimated surfaces of fractional photosynthetic cover and compared it to the field data, we found significant, positive correlations between estimated cover and field data at the Middle and High sites (Figure 3A). We found no significant correlations between the field data and estimated fractional photosynthetic cover at the Low site.

We identified cover types where the models performed with higher and lower uncertainty, based on the spatially explicit maps of standard deviation and coefficient of variation (Figure 4). The highest uncertainty occurred for imagery pixels of mixed soil and grass and pixels of bare soil. Pixels of dense shrub and grass had the lowest uncertainty for all sites.

Lastly, we calculated the fractional photosynthetic cover attributed to each PFT class at each site (Figure 3B). We found that the distributions of fractional photosynthetic cover values reflected the physiological characteristics of PFTs across the elevation gradient. This finding demonstrates that from UAS imagery, we capture the fine spatial scale heterogeneity of photosynthetic cover that we observe in the field between and within the sites.

Comparison of UAS imagery protocols across sites

Using the same UAS imagery protocols across a gradient of sagebrush ecosystems, we were able to successfully map PFTs and fractional photosynthetic cover at all sites. However, the correlation with field data varied between sites. The UAS image products from the Middle and High sites were significantly positively correlated with the field data (Table 3). The Low site showed no correlation between PFT fractional cover derived from UAS imagery and field data. The image products at the Low Site had high accuracy as stand-alone products, but they were not conducive to tests or comparison with the point intercept field data collected at the Low site.

When we mapped fractional photosynthetic cover, we found that for all sites, MSAVI was the vegetation index with the highest accuracy to model a relationship between the multispectral imagery and fractional photosynthetic cover. Therefore, the same UAS flight and image analysis protocols show good transferability across the landscape gradient to map fractional photosynthetic cover as stand-alone products.

DISCUSSION

We tested the assumption that the same UAS imagery protocols are transferable across an elevational gradient to map and model plant communities in the Northern Great Basin. We found strong evidence for the transferability of UAS imagery protocols to map PFTs and fractional photosynthetic cover. We found that correlation between UAS imagery and field data varied by site. Therefore, if agreement with field data is the goal, we recommend testing other field data collection methods, given the high accuracy of image products, three-fold increase in data density, and 100% plot coverage from UAS imagery. These findings highlight the benefits and potential for UAS monitoring and the areas where more research is needed.

Our results emphasize the range of vegetation metrics that can be derived from UAS flights, from discrete classes to fractional cover. As representations of ecological complexity, each potential vegetation metric has advantages and disadvantages. Our work provides an example of the capacity for UAS to provide spatially continuous maps of plant functional types (PFTs). By reducing species diversity to generalizable classes, PFTs can aid land management (Wainwright et al. 2019) and facilitate dynamic models for the global carbon cycle (Pandit et al. 2018). However, aggregating spectral information into a small number of discrete PFTs risks oversimplifying gradual changes between spatially-varying ecological communities (Hudon et al. 2021). In contrast, continuous measurements of fractional photosynthetic cover are well-suited to represent gradual change. In this study, we identified a vegetation index (Modified Soil Adjusted

Vegetation Index; MSAVI) that was highly correlated with fractional photosynthetic cover across disparate sites. Vegetation indices have proven indispensable for analyses of coarser resolution imagery, including images acquired from satellite platforms (Bannari et al. 1995) and occupied aerial vehicles (Dahlin et al. 2014). We propose that vegetation indices, such as MSAVI, are well-poised to aid spatial and temporal comparisons for UAS imagery. An overall advantage of multispectral UAS imagery is the wealth of ecologically-relevant data products that can be derived from flights, including both discrete and continuous vegetation metrics.

Mapping plant functional types

For the PFT classified imagery, we found the strongest correlation with UAS and field data at the Middle site and no correlation at the Low site. Despite the fine spatial resolution imagery that we used to develop our training and test data, many of the forbs and grasses at our sites were too small to classify or count confidently. There was a high proportion of grass plants of less than 5cm diameter in all the sites, and these plants are not resolved because of the flight height limitation of the multispectral imagery; flying lower than 45m AGL will result in poor alignment of bands. Thus, errors of omission occurred for grasses in UAS classifications relative to field-based classification. The structural properties of some of the grasses and forbs are such that <1cm/pixel could be required to resolve these plants as features for classification. We would likely need to fly at a lower altitude in the sites described here or with a different sensor to resolve the smallest plant types like grasses and forbs. The most appropriate scale remains unclear, as a segmented feature at one scale can be homogeneous but heterogeneous when viewed at a different scale (Hossain and Chen 2019). Detecting and differentiating between soil, forbs and grasses is a continual challenge for remote sensing in drylands (Gillan et al. 2014, Dashti et al. 2019). Classification results would likely be different if we had UAS imagery

throughout the growing season, since multiple studies have shown improvements in classification accuracy due to unique phenology of plant species (Dudley et al. 2015, Chen et al. 2017, Lu et al. 2017). Our results would also likely be improved with the inclusion of structural data which can be acquired from UAS imagery via structure-for-motion algorithms (Gillan et al. 2020). In this study, we did not include structural data as computing the structure-for-motion point cloud can be computationally and time intensive, which may be a limitation for user groups who wish to apply these drone imagery protocols. Nevertheless, UAS-derived structural measurements can accurately represent plant height and aboveground biomass in dryland ecosystems (Cunliffe et al. 2016, Howell et al. 2020) and would likely improve classification accuracy of PFTs.

Sagebrush shrubs play a key role in ecosystem processes in the high deserts of western North America and we want to highlight the potential for mapping this specific plant type. The shrub class of PFT had the highest user accuracy across all three sites: Low (74%), Middle (67%), and High (62% for sagebrush, 80% for snowberry). Woody shrubs function as islands of fertility in arid ecosystems, and as such, they promote soil carbon storage and provide a niche for other native plants and microbes (Ochoa-Hueso et al. 2018). PFT maps could be used to monitor shrub cover and structure over time. Soil samples associated with known shrub locations would allow for the creation of an interpolated map of the microbial community linked to PFTs that facilitate soil stabilization, water movement and storage, and nitrogen fixation (Kattenborn et al. 2019). From the structure of the individual plant to the composition within a community, shrubs provide insights into ecosystem productivity in the Northern Great Basin.

Mapping fractional photosynthetic cover

The models to estimate fractional photosynthetic cover performed best on pixels over homogeneous and continuous ground cover, including dense shrubs and large forbs. However,

the most common ground cover in drylands is heterogeneous, a mix of soil, plant litter, and small grasses and forbs. This finding is similar to the results of UAS based measurements of fractional vegetation cover in Tibetan grasslands where model performance was best over more homogeneous areas (Chen et al. 2016). We partially attribute the strong positive correlation between field and UAS data at the Middle site to the inherent structural properties of the plant community. The shrubs, grasses, and forbs are all relatively short and dense at the Middle site; the average height of grasses is 15cm (±13.8cm), and the shrubs are 36cm (±12.5cm). In contrast to the other sites, the shrubs at the Middle site are so short that few forbs and grasses grow beneath them – there is little to no understory and less background noise from bare soil. As a result, the UAS and field methods are well correlated because the sampling environments are the most structurally homogeneous.

The model estimates of fractional photosynthetic cover for each of our sites are 24% higher than the field data. This result is likely due to the difference in sampling resolution between the field and image data. Green vegetation is less likely to be underestimated because of the high sampling resolution and spectral data from the UAS imagery. For example, soil biocrusts, a critically important feature in drylands ecosystems, are detectable in UAS imagery (Havrilla et al. 2020), but may not be recorded in point frame field plots. We also note that the UAS imagery covered the entirety of the 1ha sites, while the field plots covered 0.3% of each site. We found that the UAS pixel density was 3x higher per m^2 than the point frame field measurement density. Compared to UAS data, point-intercept data collection has low sampling density and coverage. There is an overwhelming benefit to increased spatial extent and sampling density because of linkages between remotely sensed FPC and ecosystem processes (Lehnert et al. 2015).

The fractional photosynthetic cover imagery could provide detailed spatial distribution data for future studies that relate to phenology and energy fluxes in drylands. Similar to sites in the National Ecological Observatory Network, the location of our study sites in proximity to eddy covariance flux towers is ideal for merging remotely sensed temporal measurements of fractional photosynthetic cover with GPP fluxes at the towers. Increased spatial extent and sampling density are advantageous for studies that seek to link remotely sensed fractional photosynthetic cover and ecosystem processes (Lehnert et al. 2015). There is a need for further investigation between flux tower measurements and the utilization of vegetation indices to understand better the mechanisms of the terrestrial carbon cycle (Xiao et al. 2019), as the structural diversity and distribution of plants play an important role in heat fluxes and carbon exchange (Griebel et al. 2020). These methods could be extended over time to track and analyze the impacts of global change on plant communities in drylands or other sparsely vegetated ecosystems.

Methods agreement between UAS data products and point-intercept data

In this study, we compared UAS data products to point-intercept data collected in 1 m^2 field plots. While correlations between field and remotely sensed data were generally strong, discrepancies between methods, particularly at the Low Site, indicate the need for field validation methods specifically aimed at ground-truthing UAS imagery. Point-intercept methods are a classic and widely used approach to quantifying vegetation density and cover in the field (Clark and Seyfried 2001), yet present some disadvantages for comparison with spatially-continuous UAS data products. The resolution of our UAS products was much finer than the point-intercept plots, with around 800 pixels within a single field plot, introducing potential mismatches due to aggregation. Direct observation of photosynthetic cover is also subject to

human bias, for example, decisions on whether a yellow leaf counts as photosynthetic or not. In contrast, sensor-based observations present continuous measurements of greenness that can reduce bias (Fisk et al. 2019). Despite these challenges, we believe comparisons of UAS data products and traditional field methods are still valuable, for example to understand how contemporary UAS imagery relates to historical data. For optimal comparisons of on-the-ground data and UAS imagery, field methods that record the precise location of different plant species and cover types may be more valuable than plot-based methods (Gillan et al. 2020). Tradeoffs in allocating effort towards different field methods warrant further investigation as remotely sensed measurements become integrated into networks of long-term monitoring sites (Kitzes et al. 2021).

Comparing UAS imagery protocols

We used the same UAS flight and image analysis protocols to create maps of PFTs and fractional photosynthetic cover across an elevational and precipitation gradient of sagebrush ecosystems. Despite the differences in sagebrush subspecies communities, we were able to map and quantify commonly used ecological metrics. We found our protocols for mapping shrub classes had the greatest transferability across an elevation gradient, which is broadly applicable given the integral presence of sagebrush in the Great Basin. When planning UAS surveys, it is critical to define the desired end products before the flights occur and answer questions including: what is the smallest plant that needs to be resolved in the imagery? Are additional spectral data needed? As many replicated field sites transition to UAS use, consideration of the end goals and transferability of UAS imagery protocols will maximize per flight efficiency of data collection, processing, and analysis. While sagebrush ecosystems are the focus of this paper, our methods, analyses, and lessons learned are widely applicable to ecosystems with fine-scale

heterogeneity in vegetation structure, from arctic tundra (Fraser et al. 2016) to lava flows undergoing primary succession (Larrue et al. 2020).

Conclusions

In this study of sagebrush ecosystems, we investigated whether the same UAS imagery protocols were transferable along an elevational and precipitation gradient. We assessed the accuracy of classified PFT and estimated fractional photosynthetic cover maps. The same UAS imagery protocols were transferable across the landscape gradient for the accuracy of the maps. In contrast, the correlation between the field data and UAS imagery was inconsistent between sites. For maps of PFTs, sites with small forbs and grass and a high amount of bare ground likely required pixel resolution of less than 1cm to achieve stronger agreement with field data. UAS imagery can be used to model fractional photosynthetic cover at fine spatial scale resolution, with coverage and sampling density that greatly exceeds field data. This is a key advantage in ecosystems where individual plant cover varies at scales far below the applicability of satellite platforms. Lastly, linking the PFT imagery with fractional photosynthetic cover imagery allowed us to estimate the variation of contributions of PFTs to fractional photosynthetic cover at peak biomass. Altogether, our results speak to the great promise of UAS for spatially extensive, continuous measurements of fine-scale variation in ecosystem structure. The time is right to implement UAS as a standard tool for monitoring.

ACKNOWLEDGMENTS

We would like to thank the USDA Agriculture Research Service under Cooperative Agreement 59-2052-8-002 for funding this project, and providing resources and access to the study sites in Reynolds Creek Experimental Watershed. This publication was also made possible

by the NSF Idaho EPSCoR Program and by the National Science Foundation under award number OIA-1757324. TTC was supported by NSF award number DEB-2207158.

AUTHOR CONTRIBUTIONS

Anna Roser, Nancy Glenn, Trevor Caughlin, Marie-Anne de Graaff, Pat Clark, Fred Pierson, Alex Boehm, and Josh Enterkine conceived the ideas and designed methodology; Anna Roser, Alex Boehm and USDA ARS vegetation team collected the data; Anna Roser, Juan M. Requena-Mullor, and Trevor Caughlin analyzed the data; Anna Roser, Nancy Glenn, Pat Clark, and Trevor Caughlin led the writing of the manuscript. All authors contributed critically to the drafts and gave final approval for publication.

CONFLICT OF INTEREST

The authors declare no conflict of interest.

DATA AVAILABILITY STATEMENT

Data are available from the U.S. Department of Agriculture's Ag Data Commons (Clark 2022a, 2022b); point intercept data: https://doi.org/10.15482/USDA.ADC/1527856; drone imagery data: https://doi.org/10.15482/USDA.ADC/1528092.

REFERENCES

Bannari, A., D. Morin, F. Bonn, and A. R. Huete. 1995. A review of vegetation indices. Remote Sensing Reviews 13:95–120.

Baret, F., and G. Guyot. 1991. Potentials and limits of vegetation indices for LAI and APAR assessment. Remote Sensing of Environment 35:161–173.

Beckstead, J., S. E. Meyer, B. M. Connolly, M. B. Huck, and L. E. Street. 2010. Cheatgrass facilitates spillover of a seed bank pathogen onto native grass species: Indirect influence of seed bank pathogen loads. Journal of Ecology 98:168–177.

Bickel, J. E. 2007. Some Comparisons among Quadratic, Spherical, and Logarithmic Scoring Rules. Decision Analysis 4:49–65.

Brantley, S. L., W. H. McDowell, W. E. Dietrich, T. S. White, P. Kumar, S. P. Anderson, J. Chorover, K. A. Lohse, R. C. Bales, D. D. Richter, G. Grant, and J. Gaillardet. 2017. Designing a network of critical zone observatories to explore the living skin of the terrestrial Earth. Earth Surface Dynamics 5:841–860.

Breulmann, M., E. Schulz, K. Weißhuhn, and F. Buscot. 2012. Impact of the plant community composition on labile soil organic carbon, soil microbial activity and community structure in semi-natural grassland ecosystems of different productivity. Plant and Soil 352:253–265.

Caughlin, T. T., C. Barber, G. P. Asner, N. F. Glenn, S. A. Bohlman, and C. H. Wilson. 2021. Monitoring tropical forest succession at landscape scales despite uncertainty in Landsat time series. Ecological Applications 31:e02208.

Chen, B., B. Huang, and B. Xu. 2017. Multi-source remotely sensed data fusion for improving land cover classification. ISPRS Journal of Photogrammetry and Remote Sensing 124:27–39.

Chen, J., S. Yi, Y. Qin, and X. Wang. 2016. Improving estimates of fractional vegetation cover based on UAV in alpine grassland on the Qinghai–Tibetan Plateau. International Journal of Remote Sensing 37:1922–1936.

Chen, N., K. Yu, R. Jia, J. Teng, and C. Zhao. 2020. Biocrust as one of multiple stable states in global drylands. Science Advances 6:eaay3763.

Clark, P. 2022a. Data from: UAS imagery protocols to map vegetation are transferable between dryland sites across an elevational gradient. Ag Data Commons. https://doi.org/10.15482/USDA.ADC/1527856

Clark, P. 2022b. UAS imagery protocols to map vegetation are transferable between dryland sites across an elevational gradient. Ag Data Commons. https://doi.org/10.15482/USDA.ADC/1528092

Clark, P. E., and M. S. Seyfried. 2001. Point Sampling for Leaf Area Index in Sagebrush Steppe Communities. Journal of Range Management 54:589.

Cunliffe, A. M., R. E. Brazier, and K. Anderson. 2016. Ultra-fine grain landscape-scale quantification of dryland vegetation structure with drone-acquired structure-from-motion photogrammetry. Remote Sensing of Environment 183:129–143.

Dahlin, K. M., G. P. Asner, and C. B. Field. 2014. Linking vegetation patterns to environmental gradients and human impacts in a mediterranean-type island ecosystem. Landscape Ecology 29:1571–1585.

Dashti, H., A. Poley, N. F. Glenn, N. Ilangakoon, L. Spaete, D. Roberts, J. Enterkine, A. N. Flores, S. L. Ustin, and J. J. Mitchell. 2019. Regional scale dryland vegetation classification with an integrated lidar-hyperspectral approach. Remote Sensing 11.

Dudley, K. L., P. E. Dennison, K. L. Roth, D. A. Roberts, and A. R. Coates. 2015. A multi-temporal spectral library approach for mapping vegetation species across spatial and temporal phenological gradients. Remote Sensing of Environment 167:121–134.

Fraser, R. H., I. Olthof, T. C. Lantz, C. Schmitt, R. H. Fraser, I. Olthof, and C. Schmitt. 2016. UAV photogrammetry for mapping vegetation in the low-Arctic. Arctic Science 2:79–102.

Gillan, J. K., J. W. Karl, M. Duniway, and A. Elaksher. 2014. Modeling vegetation heights from high resolution stereo aerial photography: An application for broad-scale rangeland monitoring. Journal of Environmental Management 144:226–235.

Gillan, J. K., J. W. Karl, and W. J. D. van Leeuwen. 2020. Integrating drone imagery with existing rangeland monitoring programs. Environmental monitoring and assessment 192:269.

Gitelson, A. A., and M. N. Merzlyak. 1998. Remote sensing of chlorophyll concentration in higher plant leaves. Advances in Space Research 22:689–692.

Griebel, A., D. Metzen, M. M. Boer, C. V. M. Barton, A. A. Renchon, H. M. Andrews, and E. Pendall. 2020. Using a paired tower approach and remote sensing to assess carbon sequestration and energy distribution in a heterogeneous sclerophyll forest. Science of The Total Environment 699:133918.

Havrilla, C. A., M. L. Villarreal, J. L. DiBiase, M. C. Duniway, and N. N. Barger. 2020. Ultra-high-resolution mapping of biocrusts with Unmanned Aerial Systems. Remote Sensing in Ecology and Conservation 6:441–456.

Hossain, M. D., and D. Chen. 2019. Segmentation for Object-Based Image Analysis (OBIA): A review of algorithms and challenges from remote sensing perspective. ISPRS Journal of Photogrammetry and Remote Sensing 150:115–134.

Howell, R. G., R. R. Jensen, S. L. Petersen, and R. T. Larsen. 2020. Measuring Height Characteristics of Sagebrush (Artemisia sp.) Using Imagery Derived from Small Unmanned Aerial Systems (sUAS). Drones 4:6.

Hudon, S. F., A. Zaiats, A. Roser, A. Roopsind, C. Barber, B. C. Robb, B. A. Pendleton, M. J. Camp, P. E. Clark, M. M. Davidson, J. Frankel-Bricker, M. Fremgen-Tarantino, J. S. Forbey, E. J. Hayden, L. A. Richards, O. K. Rodriguez, and T. T. Caughlin. 2021. Unifying community detection across scales from genomes to landscapes. Oikos 130:831–843.

Kattenborn, T., F. E. Fassnacht, and S. Schmidtlein. 2019. Differentiating plant functional types using reflectance: which traits make the difference? Remote Sensing in Ecology and Conservation 5:5–19.

Kitzes, J., R. Blake, S. Bombaci, M. Chapman, S. M. Duran, T. Huang, M. B. Joseph, S. Lapp, S. Marconi, W. K. Oestreich, T. A. Rhinehart, A. K. Schweiger, Y. Song, T. Surasinghe, D. Yang, and K. Yule. 2021. Expanding NEON biodiversity surveys with new instrumentation and machine learning approaches. Ecosphere 12:e03795.

Koh, L. P., and S. A. Wich. 2012. Dawn of Drone Ecology: Low-Cost Autonomous Aerial Vehicles for Conservation. Tropical Conservation Science 5:121–132.

Koutroulis, A. G. 2019. Dryland changes under different levels of global warming. Science of The Total Environment 655:482–511.

Larrue, S., R. Paris, and S. Etienne. 2020. The use of vascular plant densities to estimate the age of undated lava flows in semi-arid areas of Fogo Island (Cape Verde, Atlantic Ocean). Journal of Arid Environments 173:104042.

Lehnert, L. W., H. Meyer, Y. Wang, G. Miehe, B. Thies, C. Reudenbach, and J. Bendix. 2015. Retrieval of grassland plant coverage on the Tibetan Plateau based on a multi-scale, multi-sensor and multi-method approach. Remote Sensing of Environment 164:197–207.

Lu, M., B. Chen, X. Liao, T. Yue, H. Yue, S. Ren, X. Li, Z. Nie, and B. Xu. 2017. Forest Types Classification Based on Multi-Source Data Fusion. Remote Sensing 9:1153.

Marvin, D. C., L. P. Koh, A. J. Lynam, S. Wich, A. B. Davies, R. Krishnamurthy, E. Stokes, R. Starkey, and G. P. Asner. 2016. Integrating technologies for scalable ecology and conservation. Global Ecology and Conservation 7:262–275.

McFeeters, S. K. 1996. The use of the Normalized Difference Water Index (NDWI) in the delineation of open water features. International Journal of Remote Sensing 17:1425–1432.

Ning, Z., X. Zhao, Y. Li, L. Wang, J. Lian, H. Yang, and Y. Li. 2021. Plant community C:N:P stoichiometry is mediated by soil nutrients and plant functional groups during grassland desertification. Ecological Engineering 162:106179.

Ochoa-Hueso, R., D. J. Eldridge, M. Delgado-Baquerizo, S. Soliveres, M. A. Bowker, N. Gross, Y. Le Bagousse-Pinguet, J. L. Quero, M. García-Gómez, E. Valencia, T. Arredondo, L. Beinticinco, D. Bran, A. Cea, D. Coaguila, A. J. Dougill, C. I. Espinosa, J. Gaitán, R. T. Guuroh, E. Guzman, J. R. Gutiérrez, R. M. Hernández, E. Huber-Sannwald, T. Jeffries, A. Linstädter, R. L. Mau, J. Monerris, A. Prina, E. Pucheta, I. Stavi, A. D. Thomas, E.

Zaady, B. K. Singh, and F. T. Maestre. 2018. Soil fungal abundance and plant functional traits drive fertile island formation in global drylands. Journal of Ecology 106:242–253.

Olsoy, P. J., L. A. Shipley, J. L. Rachlow, J. S. Forbey, N. F. Glenn, M. A. Burgess, and D. H. Thornton. 2018. Unmanned aerial systems measure structural habitat features for wildlife across multiple scales. Methods in Ecology and Evolution 9:594–604.

Pandit, K., H. Dashti, N. F. Glenn, A. N. Flores, K. C. Maguire, D. J. Shinneman, G. N. Flerchinger, and A. W. Fellows. 2018. Optimizing shrub parameters to estimate gross primary production of the sagebrush ecosystem using the Ecosystem Demography (EDv2. 2) model, Geosci. Model Dev. Discuss. Geoscientific Model Development Discussions:1–23.

Philip, S. Y., S. F. Kew, G. J. Van Oldenborgh, W. Yang, G. A. Vecchi, F. S. Anslow, S. Li, S. I. Seneviratne, L. N. Luu, J. Arrighi, R. Singh, V. Aalst, M. Hauser, D. L. Schumacher, C. P. Marghidan, K. L. Ebi, R. Vautard, J. Tradowsky, D. Coumou, F. Lehner, C. Rodell, R. Stull, R. Howard, N. Gillett, and F. E. L. Otto. 2021. Rapid attribution analysis of the extraordinary heatwave on the Pacific Coast of the US and Canada June 2021 . https://www.worldweatherattribution.org/wp-content/uploads/NW-US-extreme-heat-2021-scientific-report-WWA.pdf.

Polley, H. W., C. A. Kolodziejczyk, K. A. Jones, J. D. Derner, D. J. Augustine, and D. R. Smith. 2022. UAV−Enabled Quantification of Grazing-Induced Changes in Uniformity of Green Cover on Semiarid and Mesic Grasslands. Rangeland Ecology & Management 80:68–77.

Poulter, B., D. Frank, P. Ciais, R. B. Myneni, N. Andela, J. Bi, G. Broquet, J. G. Canadell, F. Chevallier, Y. Y. Liu, S. W. Running, S. Sitch, and G. R. Van Der Werf. 2014.

Contribution of semi-arid ecosystems to interannual variability of the global carbon cycle. Nature 509:600–603.

Qi, J., A. Chehbouni, A. R. Huete, Y. H. Kerr, and S. Sorooshian. 1994. A modified soil adjusted vegetation index. Remote sensing of environment 48:119–126.

Renne, R. R., D. R. Schlaepfer, K. A. Palmquist, J. B. Bradford, I. C. Burke, and W. K. Lauenroth. 2019. Soil and stand structure explain shrub mortality patterns following global change–type drought and extreme precipitation. Ecology 100:1–17.

Rominger, K., and S. E. Meyer. 2019. Application of UAV-Based Methodology for Census of an Endangered Plant Species in a Fragile Habitat. Remote Sensing 11:719.

Rondeaux, G., M. Steven, and F. Baret. 1996. Optimization of soil-adjusted vegetation indices. Remote sensing of environment 55:95–107.

Rouse Jr, J. W., R. H. Haas, D. W. Deering, J. A. Schell, and J. C. Harlan. 1974. Monitoring the vernal advancement and retrogradation (green wave effect) of natural vegetation.

Shriver, R. K., C. M. Andrews, R. S. Arkle, D. M. Barnard, M. C. Duniway, M. J. Germino, D. S. Pilliod, D. A. Pyke, J. L. Welty, and J. B. Bradford. 2019. Transient population dynamics impede restoration and may promote ecosystem transformation after disturbance. Ecology Letters 22:1357–1366.

Vivoni, E. R., E. R. Pérez-Ruiz, Z. T. Keller, E. A. Escoto, R. C. Templeton, N. P. Templeton, C. A. Anderson, A. P. Schreiner-McGraw, L. A. Méndez-Barroso, A. Robles-Morua, R. L. Scott, S. R. Archer, and D. P. C. Peters. 2021. Long-term research catchments to investigate shrub encroachment in the Sonoran and Chihuahuan deserts: Santa Rita and Jornada experimental ranges. Hydrological Processes 35:e14031.

Wainwright, C. E., G. M. Davies, E. Dettweiler-Robinson, P. W. Dunwiddie, D. Wilderman, and J. D. Bakker. 2019. Methods for tracking sagebrush-steppe com munity trajectories and quantifying resilience in relation to disturbance and restoration. Restoration Ecology 28:115–126.

Wood, D. J. A., T. M. Preston, S. Powell, and P. C. Stoy. 2022. Multiple UAV Flights across the Growing Season Can Characterize Fine Scale Phenological Heterogeneity within and among Vegetation Functional Groups. Remote Sensing 14:1290.

Woodward, F. I., and W. Cramer. 1996. Plant functional types and climatic change: Introduction. Journal of Vegetation Science 7:306–308.

Xiao, J., F. Chevallier, C. Gomez, L. Guanter, J. A. Hicke, A. R. Huete, K. Ichii, W. Ni, Y. Pang, A. F. Rahman, G. Sun, W. Yuan, L. Zhang, and X. Zhang. 2019. Remote sensing of the terrestrial carbon cycle: A review of advances over 50 years. Remote Sensing of Environment 233:111383.

TABLES AND FIGURE LEGENDS

Table 1. Details of UAS collection at each site and flight parameters used.

Sensor	**GSD (cm/pixel)**	**AGL (m)**	**Reconstruction error (cm)**	**Slidelap (%)**	**Speed (m/s)**	**Date**
Low site						
MicaSense Rededge	4.50	75	2.7	70	3	6/5/2019
RGB Phantom	0.70	20	0.7	80	6	6/4/2019
Middle site						
MicaSense Rededge	4.0	60	2.4	75	3	6/25/2019
RGB Phantom	0.8	20	0.5	80	6	6/25/2019
High site						
MicaSense Rededge	4.0	60	2.6	75	3	7/9/2019
RGB Phantom	0.8	20	0.5	80	6	7/2/2019

Note: Reconstruction error refers to the accuracy of point positioning in pixel units.

Table 2. Spectral vegetation indices and formulas used in this study.

Vegetation index	Acronym	Source	Equation
Normalized difference vegetation index	NDVI	Rouse Jr. et al. 1974	(NIR−Red)/(NIR+Red)
Modified soil adjusted vegetation index	MSAVI	Qi et al. 1994	NIR+0.5−(0.5∗sqrt((2∗NIR+1)2−8∗(NIR−(2∗Red))))
Optimized soil adjusted vegetation index	OSAVI	Rondeaux et al. 1996	((NIR - Red)/(NIR + Red + 0.16))*(1 + 0.16)
Green normalized vegetation index	GNDVI	Gitelson and Merzlyak 1998	(NIR−Green)/(NIR+Green)
Normalized difference water index	NDWI	McFeeters 1996	(Green−NIR)/(Green+NIR)
Normalized ratio vegetation index	NRVI	Baret and Guyot 1991	(Red/NIR−1)/(Red/NIR+1)

Table 3. Summary of rho (r) and RMSD values for each site and each correlation test for PFTs (asterisk indicates statistical significance).

Statistic	**Shrubs**	**Grass**	**Ground**	**Forbs**
Low site				
r	0.1	0.18	0.17	
RMSD	0.32	0.32	0.4	
Middle site				
r	0.83*	0.3	0.7*	0.94*
RMSD	0.11	0.2	0.21	0.05
High site				
r	0.58*	0.32	0.61*	0.39*
RMSD	0.25	0.21	0.39	0.13

Note: Forbs are not included for the Low site because they were too small to be resolved in the RGB or multispectral imagery.

Table 4. Summary of predictive capacity of vegetation indices to predict fractional photosynthetic cover across sites. Lower log-loss and higher average accuracy indicate better performance.

Statistic	**NDVI**	**GNDVI**	**MSAVI**	**OSAVI**	**NDWI**	**NRVI**
Low site						
Average accuracy	80	72	80	80	72	80
Log-loss metric	0.40	0.52	0.40	0.40	0.52	0.40
Middle site						
Average accuracy	63	61	64	63	61	63
Log-loss metric	0.59	0.61	0.58	0.59	0.61	0.59
High site						
Average accuracy	93	89	93	93	89	93
Log-loss metric	0.16	0.23	0.16	0.16	0.23	0.16

Figures

Figure 1. Elevation map of Reynolds Creek Experimental Watershed, with site location within Idaho. The study sites, along the elevational gradient are marked with colored circles: Low site (pink), Middle site (blue), and High site (green). UAS true color imagery is shown from the Middle site with the plot footprint (black) and field plots (yellow) displayed.

Figure 2. Photos of study sites. For reference, the plastic white frame is 1 m^2. At the Low site (elevation: 1,425 m), note the large amount of bare ground with interspersed grasses and shrubs. The Middle site (elevation: 1,680 m) is characterized by shrubs, forbs, and grasses that are short and dense. At the High site (elevation 2,110 m), the shrubs are tall and there is less bare ground because there are many forbs and grasses that are dispersed rather than bunched. Below the photos, a matrix of nine images shows: true color imagery, classified imagery, and fractional photosynthetic cover imagery for each site at the same plot, respectively.

Figure 3. (A) Scatterplots of fractional photosynthetic cover for each site from field and remotely sensed data. UAS stands for unoccupied aerial systems. 50% and 95% Confidence Intervals are shown as blue ellipses. Rho (r) and root mean square differences calculated from UAS and field estimates of fractional photosynthetic cover. (B) For each site, the bar plots represent the mean fractional photosynthetic values for randomly selected classified plant functional types (n = 800 per site). At the Middle site, mean values for Grass and Ground are nearly the same, indicating high variability of fractional photosynthetic cover in these classes. In contrast, Forbs and Trees have high mean values, indicating less variability in photosynthetic cover for those classes. The spatial heterogeneity of sagebrush ecosystems is reflected in the variation of values between site and plant functional type. In the High site, sage and snowberry are presented separately because they are spectrally distinct.

Figure 4. Example of the variability of the model to map fractional photosynthetic cover at 1-m^2 scale (black box) at a Middle site plot. Clockwise from the top left: True color, estimated photosynthetic cover, standard deviation of photosynthetic cover, and coefficient of variation of photosynthetic cover. Darker pixels represent higher values. The highest values of variation are pixels over heterogeneous and bare soil cover types.

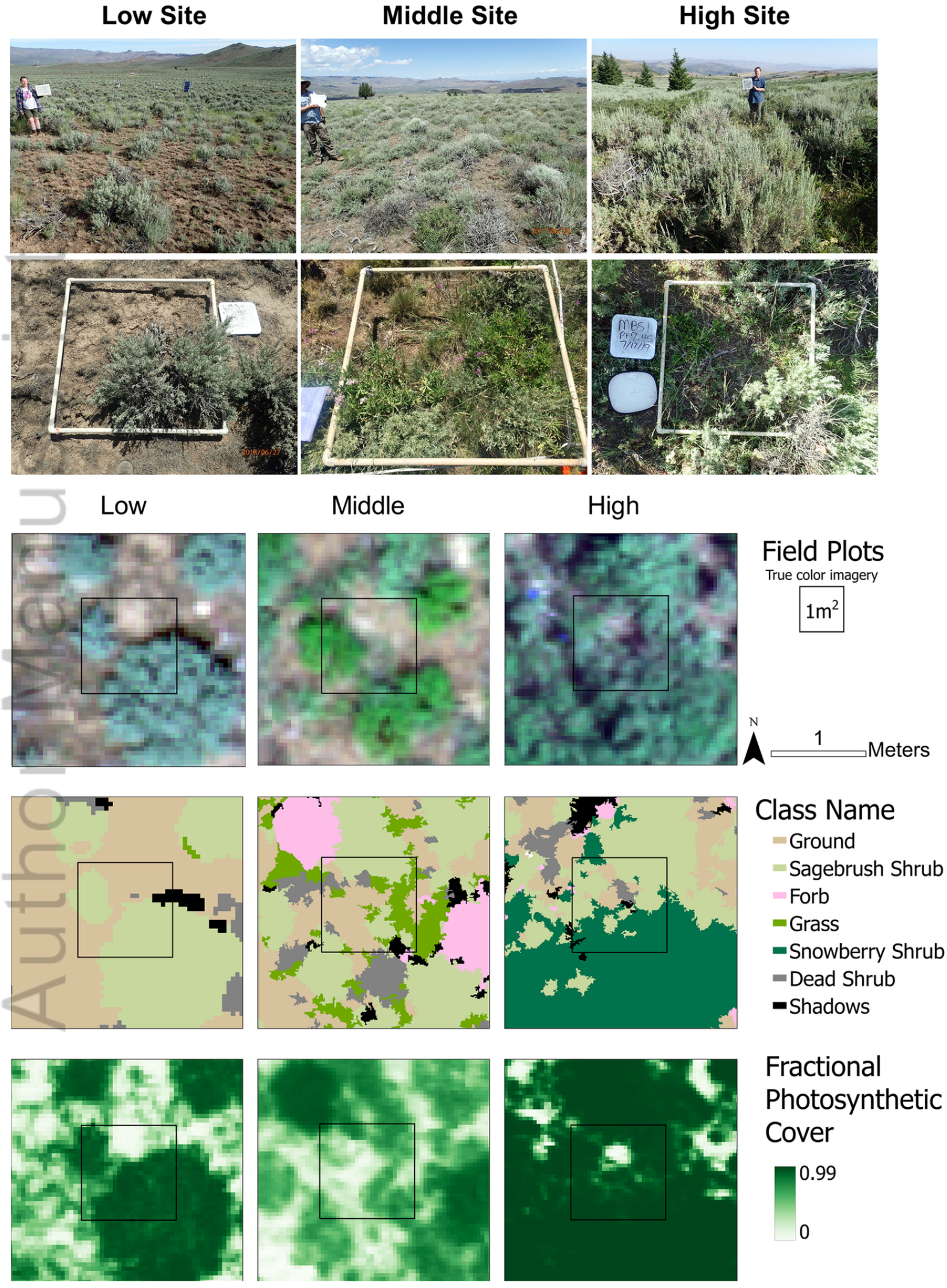

ECS2_4330_Caughlin ECS22-0348 Fig 2.png